Journal of Power Sources 263 (2014) 85–89

Contents lists available at ScienceDirect

Journal of Power Sources

journal homepage: www.elsevier.com/locate/jpowsour

Short communication

Flexible self-standing graphene–Se@CNT composite film as a binder-free cathode for rechargeable Li–Se batteries

Kai Han [a], Zhao Liu [b], Hongqi Ye [a,*], Fang Dai [c,*]

[a] College of Chemistry and Chemical Engineering, Central South University, Changsha 410083, China
[b] Department of Material Science and Engineering, Northwestern University, Evanston, IL 60208, USA
[c] Optimal CAE Inc., Plymouth, MI 48170, USA

HIGHLIGHTS

- A flexible, self-standing graphene–Se@CNT composite film was synthesized.
- The film cathode delivered a high reversible discharge capacity.
- The performance is mainly attributed to synergistic effects of graphene and CNT.

ARTICLE INFO

Article history:
Received 9 March 2014
Received in revised form
25 March 2014
Accepted 7 April 2014
Available online 18 April 2014

Keywords:
Li–Se batteries
Graphene–Se@CNT composite
Self-standing
Binder-free
Cathode

ABSTRACT

A flexible, self-standing graphene–Se@CNT composite film has been synthesized by a facile two-step assembly process. The film is directly employed as cathode for rechargeable Li–Se batteries without extra binders and conductive additives. It exhibits much higher reversible capacity and cycling stability (315 mAh g^{-1} after 100 cycles at 0.1 C) than graphene–Se composite film. The improved electrochemical performance is mainly attributed to the synergistic effects of graphene and CNT, which not only function as a flexible scaffold for strains/stresses release and volume expansion, but also offer a three-dimensional conductive architecture with open channels for electron transfer and Li ion diffusion, as well as strong confinement of soluble polyselenides.

1. Introduction

Rechargeable lithium-ion (Li-ion) batteries have been widely applied for portable electronic devices in the past two decades owing to their high reversibility and long cycle life [1–3]. However, the energy density of current Li-ion batteries is insufficient to satisfy the requirements for emerging energy storage applications, such as electric vehicles and large-scale stationary grid, due to the limited capacity by metal oxide/phosphate cathodes and graphite anode [4,5]. High capacity silicon or tin materials have been successfully developed to replace carbon anode [6,7]. However, developing high-capacity cathode materials are urgently needed. Although sulfur and oxygen have high theoretical capacity reacting with lithium, both Li–S and Li–O_2 batteries suffer from poor cycling stability that prevent their practical application [8,9]. Most recently, a new class of selenium based cathode material has been explored for both rechargeable lithium and sodium batteries [10–16]. The d-electron containing selenium possesses a similar electrochemical property as sulfur that each selenium atom can react with a maximum of two lithium ions [14]. As a result, Se could provide a theoretical capacity of 675 mAh g^{-1}, much higher than that of the current cathode materials. In the meantime, the volumetric capacity of Se (3268 mAh cm^{-3}) is also exceptional, even comparable to that of S (3467 mAh cm^{-3}) due to the higher density of Se [10,11]. Moreover, the electrical conductivity of Se is approximately 20 orders of magnitude higher than S, resulting in better cycle and rate performance without needing to add large amount of conductive carbon additives [15]. These advantages make Se a new promising cathode material for high-energy rechargeable lithium batteries. However, similar to sulfur cathode, one of the biggest challenge to Se is the dissolution and migration of polyselenide in

* Corresponding authors.
E-mail addresses: hongqiye@gmail.com (H. Ye), daifang621@gmail.com (F. Dai).

http://dx.doi.org/10.1016/j.jpowsour.2014.04.027
0378-7753/

electrolyte during cycling, which result in fast capacity fading and low Coulombic efficiency, as reported for nanoporous Se cathode [12]. One reported effective solution to overcome this issue is to use mesoporous carbon, such as CMK-3, which act as a conductive matrix to retard polyselenide shuttle and further improve conductivity of Se. This type of Se–carbon composite has improved the capacity utilization and cycling stability. Nevertheless, additional binder and carbon additives are needed, resulting in a relatively low Se loading of 24% in the electrode [16]. Therefore, it is worthy of exploring binder-free Se–carbon composite materials to increase the overall energy density of the battery.

Both of graphene and carbon nanotube have excellent electrical conductivity, chemical stability and mechanical properties [17–20]. Self-standing flexible graphene film, stacked from graphene nanosheets, has been successfully applied as electrodes or scaffolds to embed electrochemical active materials, such as silicon or sulfur, for binder-free Li-ion batteries [21–23]. The elimination of binder and organic solvent during electrode fabrication not only save cost and avoid related environmental problem caused by the evaporation of organic solvent but also could effectively improve the overall battery energy density [24]. Furthermore, it has been demonstrated that constructing of graphene–CNT 3D architecture shows higher potential for energy application than individual use of graphene or CNT [17].

In this work, a flexible, self-standing graphene–Se@CNT composite film has been firstly synthesized through thermal infusion strategy together with ultra-sonication and vacuum filtration approach. In the graphene–Se@CNT composite film, Se is uniformly coated on the surface of CNT and Se@CNT composites are well embedded between graphene nanosheets, resulting in a 3D conductive network with open channels for electron transfer and Li ion diffusion, as well as strong confinement of soluble polyselenides. This free-standing composite film electrode shows a high capacity and cycling stability for rechargeable Li–Se batteries.

2. Experimental methods

2.1. Synthesis of graphene–Se@CNT composite film

A schematic of the synthesis process is shown in Fig. 1. Graphene oxide (GO) was synthesized from flake graphite using a modified Hummers method in a two oxidation steps, as reported in our previous work [25]. Se@CNT composites were prepared by a thermal infusion method. Multi-walled carbon nanotube (US Research Nanomaterials, Inc.; diameter 10–20 nm, length 10–50 μm) and Se (Sigma Aldrich) were mixed by mechanical ball milling for 72 h at 1:1 weight ratio. The mixture Se–CNT powders were then heating at 260 °C for 20 h under argon atmosphere. After cooling down, the Se@CNT composite powders were collected and typically 30 mg was dispersed in 6 mL of water/ethanol (1:1 v/v) mixture solvent and sonicated for 30 min. 6 mL of GO suspension (5 mg mL^{-1}) was added to give a GO:Se@CNT weight ratio of 1:1. The mixture was sonicated for 1 h to get stable suspension. Next, 4 mL of the GO–Se@CNT mixture suspension was vacuum filtrated with anodic aluminum oxide (AAO) membrane (Whatman, 0.2 μm pore size, 47 mm diameter) to produce a free-standing GO–Se@CNT composite film. The film was then punched into several circular disks with a diameter of 1 cm. Subsequently, the circular disks were put into a small glass vial, which was further placed in a big glass bottle containing 2 mL of hydrazine monohydrate (Sigma Aldrich), without direct contact between the film and hydrazine monohydrate. After sealing, the glass bottle was maintained at 120 °C for 3 h to reduce GO in situ by hydrazine vapor. Following cool down, the film was gently washed with distilled de-ionized (DDI) water twice to remove the adsorbed hydrazine and dried in air at room temperature overnight. Lastly, graphene–Se@CNT film was heating at 200 °C in a flow of Ar for 10 h to further reduce GO. For comparison, graphene–Se and graphene–CNT composite films were also prepared under the same condition, respectively.

2.2. Material characterization

The morphology and microstructure of the composites were examined using Hitachi S-8030 field emission scanning electron microscopy (FE-SEM) with an energy dispersive spectroscopy (EDS) detector. X-ray diffraction (XRD) patterns were collected with a Scintag XDS2000 diffractometer (Cu Kα, $\lambda = 1.5418$ Å). Raman spectra were measured on a T64000 triple Raman system using the 514.5 nm line for an Ar-ion laser as an excitation source. Thermogravimetric analyses (TGA) were performed on TGA/SDTA851e analyzer (Mettler Toledo) at a heating rate of 10 °C min^{-1} in Ar from 30 to 600 °C. X-ray photoelectron spectroscopy (XPS) was performed using an Omicron ESCA Probe equipped with an electron flood gun and Al Kα radiation (1486.6 eV) was used as an excitation source.

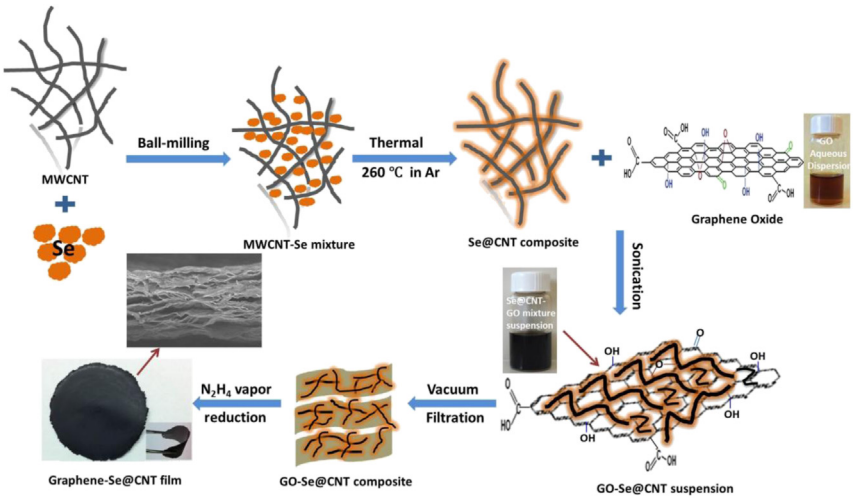

Fig. 1. Schematic illustration of the preparation process and architecture of 3D structured G–Se@CNT composite film.

2.3. Electrochemical measurements

Electrochemical measurements were conducted using two-electrode CR2032 coin cells with lithium metal as the counter electrode at room temperature. The G–Se@CNT, G–Se and G–CNT self-standing films were directly used as working electrode without any further treatment. The electrolyte was a solution of 1.2 M $LiPF_6$ dissolved in ethylene carbonate/ethylmethyl carbonate (EC/EMC, 3:7, v/v) and the separator was a Celgard 2500 film. The cells were assembled in an argon-filled glove box (H_2O, $O_2 < 1$ ppm), and galvanostatic measurements were performed on an Arbin BT2000 system in the voltage range of 1–4 V vs Li^+/Li. The *C* rate used was based on the Se theoretical capacity of 675 mAh g^{-1}. Cyclic voltammogram (CV) was recorded using the Solartron 1260/1287 electrochemical interface at a scan rate of 0.05 mV s^{-1}.

3. Results and discussion

The morphology of the graphene–Se@CNT composite film was characterized by SEM. Fig. 2a shows the graphene–Se@CNT film is self-standing and flexible, which can be bent back and forth without broken. Fig. 2b presents the high-magnification SEM image of Se@CNT composite powders with EDS elemental line scan for C and Se. After thermal infusion of Se, no bulk Se particles were observed in the Se@CNT composite (Fig. S1) and the EDS line scan revealed a uniform distribution of Se on the surface of CNT. This is in comparison with the Se–CNT mixture sample after ball-milling without thermal treatment (Fig. S2). It is noted that although the ball-milling process can help to mix the Se and CNT, the thermal infusion process is critical in uniformly coating Se on CNT surface, which is beneficial for improving Se capacity utilization as cathode material. The top-view surface images of graphene–Se@CNT composite film at low and high magnification are displayed in Fig. 2c and d. Se@CNT composites were uniformly dispersed within the graphene matrix and no large aggregates were observed. The corresponding EDS spectrum in Fig. 2c (inset) also confirmed the presence of Se within the composite film. Fig. 2e and f shows the cross-section view of the graphene–Se@CNT composite film, indicating an average thickness of about 10 μm of as-prepared film. In the high magnification image, it is observed that Se@CNT composite were well embedded between graphene nanosheets. The graphene–Se@CNT composite film has a typical sandwich-type structure with 3D conductive network composed of graphene layers and Se@CNT. The EDS elemental mapping further indicated uniform distribution of Se over the entire film in Fig. 2f (inset).

Fig. 3a presents XRD patterns of graphene–Se@CNT film, GO–Se@CNT, GO, Se@CNT, pristine CNT and Se. The characteristic diffraction peaks of Se are clearly exhibited in Se@CNT composite powders, suggesting that Se coated on CNT surface maintained its crystal structure. After incorporation with GO, the diffraction peak

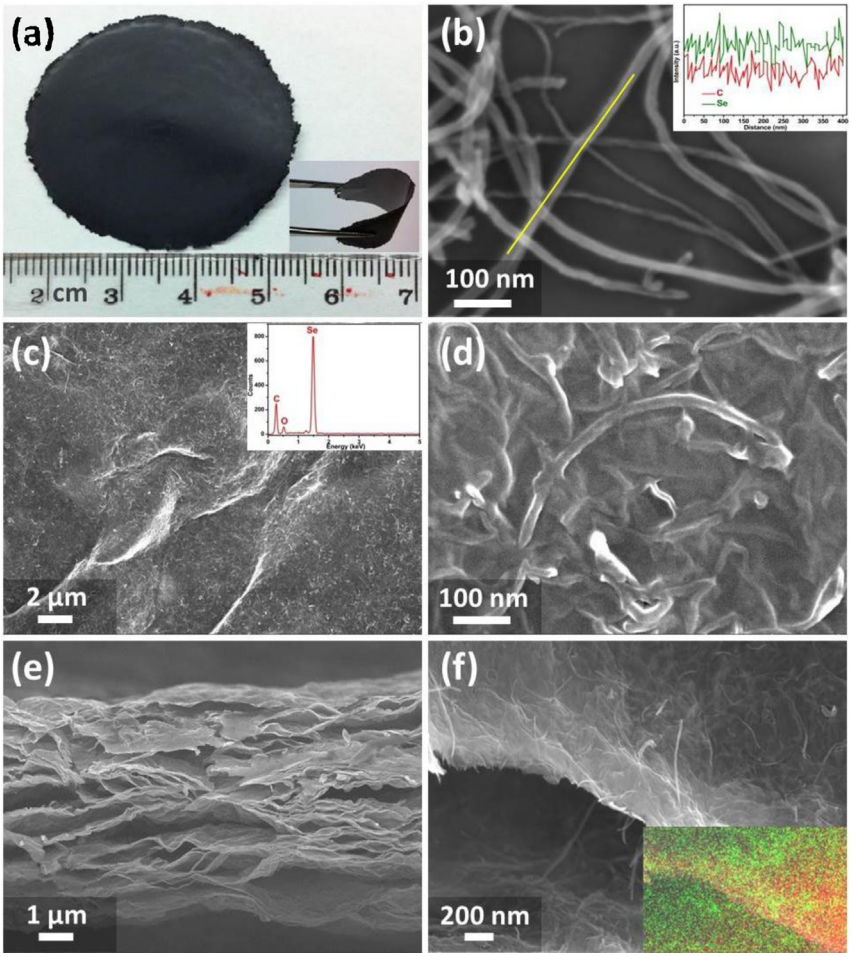

Fig. 2. (a) Digital photo of the flexible self-standing G–Se@CNT composite film; FESEM images: (b) Se@CNT composite powders with EDS line scan of C (red) and Se (green, inset); top view of G–Se@CNT composite film at low (c) and high (d) magnification with EDS elemental spectra (inset), cross-sectional views of G–Se@CNT composite film at low (e) and high (f) magnification with corresponding EDS mapping of C (red) and Se (green). (For interpretation of the references to colour in this figure legend, the reader is referred to the web version of this article.)

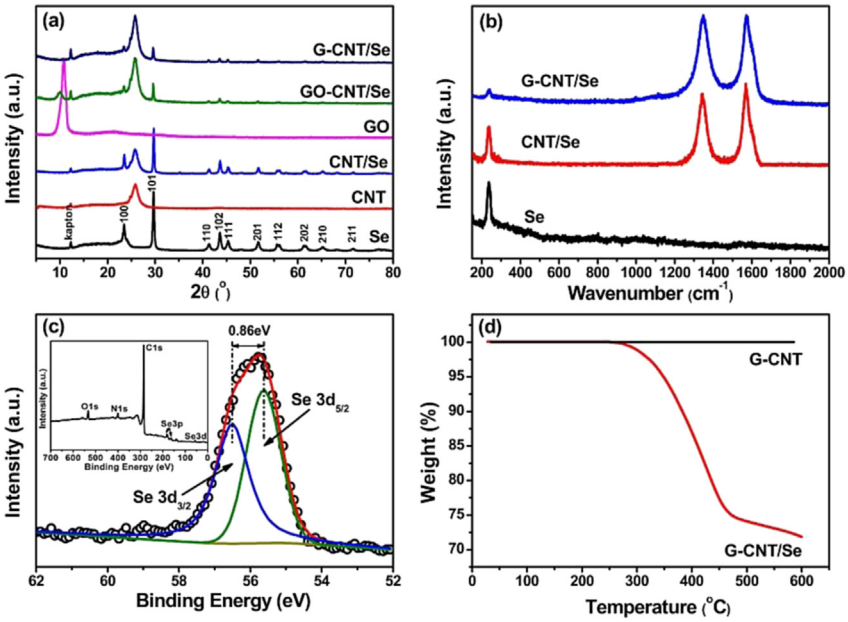

Fig. 3. (a) X-ray diffraction patterns for Se, CNT, Se@CNT, GO, GO–Se@CNT and G–Se@CNT composite film; (b) Raman spectra for Se, Se@CNT and G–Se@CNT composite film; (c) XPS spectra of high resolution Se 3d and survey scan (inset) for G–Se@CNT composite film; (d) TGA curves of G–CNT and G–Se@CNT film.

for GO at $2\theta = 10.9^\circ$ slightly shifted to 9.5°, corresponding to the increase of interlayer spacing from 0.8 nm for GO to 0.93 nm for GO–Se@CNT, which probably implies the insertion of Se@CNT into GO layers. For graphene–Se@CNT composite film, the disappearance of this peak indicated the effective reduction of GO to graphene. In addition, crystalline structure of Se in graphene–Se@CNT composite film was remained and no new phase appeared during the two-step film preparation process. The structure features of Se and carbon matrix in the composite were further probed by Raman spectroscopy (Fig. 3b). The pristine Se showed a characteristic peak at 236 cm^{-1}, corresponding to the chain-structured Se molecule [16]. Se@CNT composite powders did not show any significant change in Raman shift compared with Se, indicating the crystalline Se are physically coating on the CNT surface after thermal infusion. However, the intensity of the Se characteristic peak significantly decreased and the peak slightly blue shifted to 239 cm^{-1} in the graphene–Se@CNT composite film, suggesting the Se@CNT composite is partially embedded into graphene layers [15]. The two strong peaks at ~1350 cm^{-1} and ~1580 cm^{-1} are assigned to the D and G bands of graphene and CNT matrix, respectively, revealing that the graphene and CNT matrix were partially graphitized, which could facilitate the electron transfer from conductive carbon to Se during electrochemical reactions [17]. Besides, the intensity ratio of I_D/I_G was increased from 0.91 for Se@CNT to 1.02 for G–Se@CNT composite paper, which is resulting from the residual oxygen-containing group in graphene by reduction of GO [26]. Fig. 3c illustrates the XPS high resolution Se3d spectrum and survey scan (inset) of the graphene–Se@CNT composite film. Two peaks centered at 55.6 and 56.5 eV are clearly observed, which can be ascribed to the $3d_{5/2}$ and $3d_{3/2}$ signals of Se, indicating the presence of Se on the surface of graphene–Se@CNT film. The content of Se in the composite film was estimated to be 30 wt% by TGA, as shown in Fig. 3d.

The electrochemical performance of the self-standing graphene–Se@CNT composite film as cathode for rechargeable Li–Se batteries was evaluated using 2032-type coin cells assembled with a metallic lithium foil as counter electrode. Fig. 4a shows cyclic voltammograms of the graphene–Se@CNT composite film cathode for the initial five cycles between 1 and 4 V vs Li^+/Li at a scan rate of 0.05 mV s^{-1}. The presence of multiple pairs of reversible peaks in the CV curves indicates that the electrochemical process for the composite film is a multiple phase-change reaction [10]. Two cathodic peaks centered at 1.75 V and 1.1 V in the first cycle are corresponded to the reduction of Se to polyselenides and polyselenides to Li_2Se. Three anodic peaks were observed at 2.4 V, 3.4 V and 3.9 V in the first charging process. The two low voltage peaks could be assigned to the reverse oxidation of Li_2Se and the 3.9 V peak is probably corresponding to the partial shuttle effect of polyselenides [10]. However, after first cycle, the low cathodic peak at 1.1 V become much weaker and two new peaks at 2.75 V and 2.25 V appeared, suggesting an electrochemical activation process during the first discharge. The stable cathodic and anodic peaks in the subsequent cycles revealed good cycling stability of the graphene–Se@CNT composite film. The charge/discharge profiles of graphene–Se@CNT composite film at a current rate of 0.1 C are shown in Fig. 4b. The initial discharge displayed two slope voltage plateaus: a short one at averagely 1.75 V and a longer one at 1.1 V. This is consistent with CV curves, which also reflects the multiple phase-change reactions during the discharge. After the first cycle, the voltages of discharge plateau increased and two new plateaus at 2.75 V and 2.25 V appeared, which is probably due to the structure change of Se after the first activation process [16]. The charge curves also displayed three slope voltage plateaus like CV anodic peaks. The cycling stability of the composite film was performed at 0.1 C current rate. The film cathode delivered a reversible capacity of 400 mAh g^{-1} in the first cycle and it remained 315 mAh g^{-1} after 100 cycles with an average Coulombic efficiency above 96%. For comparison, a graphene–Se composite film was also synthesized and tested, which exhibited a discharge capacity of 100 mAh g^{-1} only for the first two cycles and then the capacity degraded rapidly to below 40 mAh g^{-1}. These results suggest that the utilization of active Se in the graphene–Se@CNT composite film has been considerably improved due to the 3D conductive network constructed by graphene and CNT. The uniform distribution of Se on CNT surface significantly improves the electrical conductivity of electrode and embedding of Se@CNT composite between graphene nanosheets produces many open channels for Li ion transfer and confinement of polyselenides. In addition, the sandwich-type

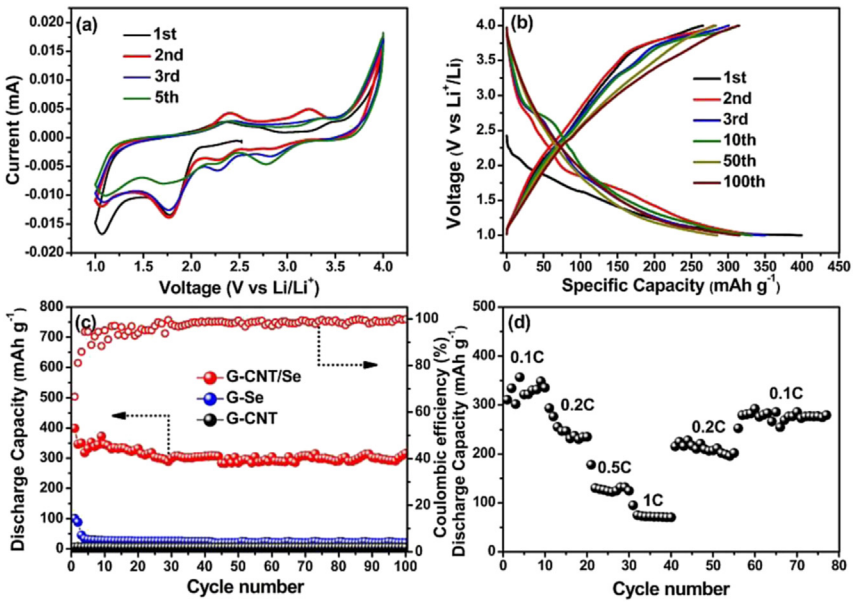

Fig. 4. (a) Cyclic voltammograms of the G–Se@CNT composite film in the initial five cycles; (b) charge/discharge profiles of the G–Se@CNT composite film with cycles at 0.1 C current rate; (c) cycling performance of the self-standing G–Se@CNT, G–Se and G–CNT films at 0.1 C; (d) rate capability of the G–Se@CNT composite film.

structure could effectively accommodate the volume variation during cycling and consequently leading to the long-term stability of Se electrode. To evaluate capacity of the carbon materials in the composite film, the pure graphene–CNT film was also tested in the same voltage range, showing almost no capacity contribution to the graphene–Se@CNT composite film. The cell also showed excellent rate capability (Fig. 4d). Capacity of 80 mAh g^{-1} was still retained at 1 C and it recovered to 280 mAh g^{-1} when the current rate was back to 0.1 C, indicating the high reversibility of the film electrode.

4. Conclusion

A flexible, self-standing graphene–Se@CNT composite film has been synthesized by a simple two-step assembly process as a binder-free cathode material for rechargeable Li–Se batteries. The composite film cathode delivers a high reversible discharge capacity of 400 mAh g^{-1} and remains 315 mAh g^{-1} even after 100 cycles with Coulombic efficiency above 96%. The highly utilization of Se in the composite film is mainly attributed to the synergistic effects of graphene and CNT, which offer a 3D conductive network with open channels not only for electron transfer and Li ion diffusion but confinement of polyselenides. Moreover, the preparation method could be easily extended to other high capacity flexible, self-standing film electrodes for energy storage applications. Also, development of such film electrodes is of great importance to enrich the research on ultra-thin and flexible batteries for soft portable electronic devices.

Acknowledgments

This work was supported by National Natural Science Foundation of China (21276284). Kai Han was supported by Hunan Provincial Innovation Foundation for Postgraduate (CX2011B081).

Appendix A. Supplementary data

Supplementary data related to this article can be found at http://dx.doi.org/10.1016/j.jpowsour.2014.04.027.

References

[1] M.S. Whittingham, Chem. Rev. 104 (2004) 4271–4302.
[2] V. Etacheri, R. Marom, R. Elazari, G. Salitra, D. Aurbach, Energy Environ. Sci. 4 (2011) 3243–3262.
[3] J.B. Goodenough, Y. Kim, Chem. Mater. 22 (2009) 587–603.
[4] M.M. Thackeray, C. Wolverton, E.D. Isaacs, Energy Environ. Sci. 5 (2012) 7854–7863.
[5] N.S. Choi, Z. Chen, S.A. Freunberger, X. Ji, Y.K. Sun, K. Amine, G. Yushin, L.F. Nazar, J. Cho, P.G. Bruce, Angew. Chem. Int. Ed. Engl. 51 (2012) 9994–10024.
[6] C.K. Chan, H. Peng, G. Liu, K. Mcllwrath, X.F. Zhang, R.A. Huggins, Y. Cui, Nat. Nanotechnol. 3 (2007) 31–35.
[7] N. Li, H. Song, H. Cui, G. Yang, C. Wang, J. Mater. Chem. A 2 (2014) 2526–2537.
[8] J. Xu, S. Dou, H. Liu, L. Dai, Nano Energy 2 (2013) 439–442.
[9] P.G. Bruce, S.A. Freunberger, L.J. Hardwick, J.M. Tarascon, Nat. Mater. 11 (2012) 19–29.
[10] A. Abouimrane, D. Dambournet, K.W. Chapman, P.J. Chupas, W. Weng, K. Amine, J. Am. Chem. Soc. 134 (2012) 4505–4508.
[11] Y. Cui, A. Abouimrane, J. Lu, T. Bolin, Y. Ren, W. Weng, C. Sun, V.A. Maroni, S.M. Heald, K. Amine, J. Am. Chem. Soc. 135 (2013) 8047–8056.
[12] L. Liu, Y. Hou, X. Wu, S. Xiao, Z. Chang, Y. Yang, Y. Wu, Chem. Commun. 49 (2013) 11515–11517.
[13] L. Liu, Y. Hou, Y. Yang, M. Li, X. Wang, Y. Wu, RSC Adv. 4 (2014) 9086–9091.
[14] D. Kundu, F. Krumeich, R. Nesper, J. Power Sources 236 (2013) 112–117.
[15] C. Yang, S. Xin, Y. Yin, H. Ye, J. Zhang, Y. Guo, Angew. Chem. Int. Ed. Engl. 52 (2013) 8363–8367.
[16] C. Luo, Y. Xu, Y. Zhu, Y. Liu, S. Zheng, Y. Liu, A. Langrock, C. Wang, ACS Nano 7 (2013) 8003–8010.
[17] R. Chen, T. Zhao, J. Lu, F. Wu, L. Li, J. Chen, G. Tan, Y. Ye, K. Amine, Nano Lett. 13 (2013) 4642–4649.
[18] J.-Z. Wang, L. Lu, M. Choucair, J.A. Stride, X. Xu, H.-K. Liu, J. Power Sources 196 (2011) 7030–7034.
[19] M. Zhao, X. Liu, Q. Zhang, G. Tian, J. Huang, W. Zhu, F. Wei, ACS Nano 6 (2012) 10759–10769.
[20] J. Kim, V.C. Tung, J. Huang, Adv. Energy Mater. 1 (2011) 1052–1057.
[21] R. Mukherjee, A.V. Thomas, A. Krishnamurthy, N. Koratkar, ACS Nano 6 (2012) 7867–7878.
[22] H. Gwon, H.-S. Kim, K.U. Lee, D.-H. Seo, Y.C. Park, Y.-S. Lee, B.T. Ahn, K. Kang, Energy Environ. Sci. 4 (2011) 1277–1283.
[23] X. Huang, B. Sun, K. Li, S. Chen, G. Wang, J. Mater. Chem. A 1 (2013) 13484–13489.
[24] W. Zhou, H. Chen, Y. Yu, D. Yang, Z. Cui, F.J. DiSalvo, H.D. Abruna, ACS Nano 7 (2013) 8801–8808.
[25] K. Han, J. Shen, C.M. Hayner, H. Ye, M.C. Kung, H.H. Kung, J. Power Sources 251 (2014) 331–337.
[26] S. Pei, J. Zhao, J. Du, W. Ren, H.-M. Cheng, Carbon 48 (2010) 4466–4474.